

MIMAC low energy electron-recoil discrimination measured with fast neutrons

Q. Riffard^a D. Santos^a O. Guillaudin^a G. Bosson^a O. Bourrion^a J. Bouvier^a
T. Descombes^a J.-F. Muraz^a L. Lebreton^b D. Maire^b P. Colas^c I. Giomataris^c
J. Busto^d D. Fouchez^d J. Brunner^d C. Tao^{d,e}

^a*LPSC, Université Grenoble-Alpes, CNRS/IN2P3, Grenoble, France*

^b*APC, Université Paris Diderot, CNRS/IN2P3, CEA/Irfu, Obs de Paris, Sorbonne Paris Cité, 75205 Paris, France*

^c*LMDN, IRSN Cadarache, 13115 Saint-Paul-Lez-Durance, France*

^d*IRFU, CEA Saclay, 91191 Gif-sur-Yvette, France*

^e*Aix Marseille Université, CNRS/IN2P3, CPPM UMR 7346, 13288, Marseille, France*

^f*Tsinghua Center for Astrophysics, Tsinghua University, Beijing 100084, China*

E-mail: riffard@apc.in2p3.fr, santos@lpsc.in2p3.fr

ABSTRACT: MIMAC (MIcro-TPC MAtrix of Chambers) is a directional WIMP Dark Matter detector project. Direct dark matter experiments need a high level of electron/recoil discrimination to search for nuclear recoils produced by WIMP-nucleus elastic scattering. In this paper, we proposed an original method for electron event rejection based on a multivariate analysis applied to experimental data acquired using monochromatic neutron fields. This analysis shows that a 10^5 rejection power is reachable for electron/recoil discrimination. Moreover, the efficiency was estimated by a Monte-Carlo simulation showing that a 10^5 electron rejection power is reached with a $86.49 \pm 0.17\%$ nuclear recoil efficiency considering the full energy range and $94.67 \pm 0.19\%$ considering a 5 keV lower threshold.

KEYWORDS: Dark Matter; directional detection; Boosted Decision Trees; electron event rejection; Neutron field; MIMAC

ARXIV EPRINT: [1602.01738](https://arxiv.org/abs/1602.01738)

Contents

1	Experimental set-up and neutron data-taking	2
1.1	The MIMAC detector	2
1.1.1	Ionization energy calibration	3
1.2	MIMAC @ AMANDE facility	4
1.2.1	Fast neutron detection	5
2	Discriminating observables	6
2.1	Minimal cuts	7
2.2	Discriminating observables	8
3	Electron/recoil discrimination by boosted decision trees	16
3.1	Boosted decision trees analysis strategy	16
3.2	BDT analysis results	18
4	BDT Analysis efficiency estimation	19
4.1	Fluorine nuclear recoil simulation	22
4.2	BDT analysis efficiency estimation	22
5	Conclusion	23

Introduction

In the standard model of cosmology the Dark Matter (DM) is about six times more abundant than the baryonic component of the matter in the Universe. Furthermore, an increasing number of astrophysical observations from local to large scales support this hypothesis. At the local scale, a dense DM halo should surround the Milky Way. Due to the relative motion of the solar system with respect to the galactic DM halo, a WIMP flux should be detected on earth. The WIMP (Weakly Interacting Massive Particle) is a massive DM particle candidate ($m_{\text{WIMP}} \sim (1 - 100\text{GeV})$) interacting only by weak and gravitational interactions. Many other DM particle candidates are proposed but the WIMP is one of the best motivated and able to be explored by direct detection. The direct detection search strategy goal is the energy spectrum measurement of nuclear recoils produced by WIMP scattering on detector target nuclei in order to constrain the DM particle properties. Direct detection experiments such as LUX [1], Xenon [2, 3], DakSide [4], EDELWEISS [5], CDMS [6], COUPP [7] and KIMS [8] put constraints on the WIMP mass, Spin Independent (SI) and Spin Dependent (SD) cross-sections. One major limitation of these search strategies arises from the neutron background. Indeed, this uncharged particle, colliding elastically with the target nuclei, will produce the same searched signal in the detector, a nuclear recoil

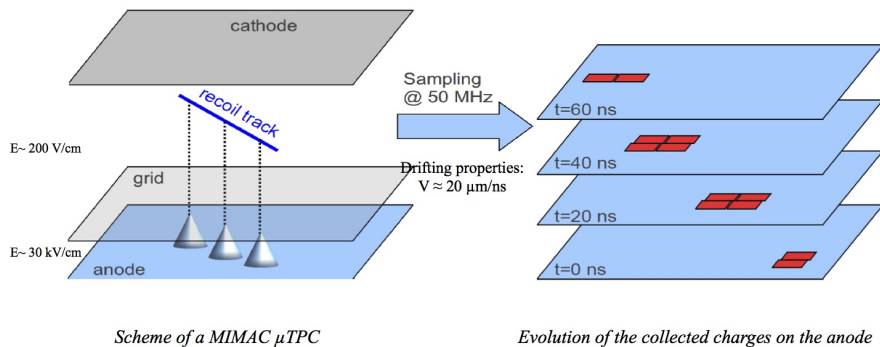


Figure 1: MIMAC detection strategy principle. The primary ionization electrons are collected to the grid and then amplified in the micromegas gap. The pixel sampling at 50 MHz allows a 3D track reconstruction.

with some tenths of keV of kinetic energy. The directional detection search strategy, first proposed in 1988 [9], is based on the angular distribution of WIMP momentum directions that should present an anisotropy in galactic coordinates. Thus, the angular distribution of recoils produced by a scattering of WIMPs on nuclei should present an anisotropy pointing towards the constellation Cygnus. Ultimate background events, mainly neutrons, should follow an isotropic distribution in galactic coordinates. Using a profile likelihood analysis [10] it has been shown that it is possible to extract a DM signal from background events. Moreover, this detection strategy can be used to constrain the DM particle and the halo properties as shown in [11].

As other directional detection experiments [12], the aim of the MIMAC project is the measurement of the nuclear recoil energies and their angular distribution to search for this signature. In order to reach this objective and before applying the directionality degree of freedom a performant electron/recoil discrimination is required. In a previous work [13], a boosted decision trees (BDT) analysis was applied on simulations to define the MIMAC low energy electron-recoil discrimination. In this paper, we propose to determine the electron/recoil discrimination from experimental data acquired with a monochromatic neutron field of 565 keV mean energy.

1 Experimental set-up and neutron data-taking

1.1 The MIMAC detector

The MIMAC detector [14] is a μ -TPC matrix of chambers filled with a low pressure (50 mbar) $\text{CF}_4 + 28\%\text{CHF}_3 + 2\%\text{C}_4\text{H}_{10}$ gas mixture. The main purpose of this detector is the measurement of nuclear recoil 3D tracks and the estimation of their kinetic energies.

As schematically illustrated in figure 1, when a charged particle or a nuclear recoil moves throughout the gas it releases part of its energy by ionization creating electron-ion pairs. These primary ionization electrons are collected, by an electric field ($E_{drift} = 180 \text{ V.cm}^{-1}$), to the grid of a pixelated bulk micromegas [15, 16] of 10.8 cm side. The 200 μm pixels are linked by strips with a 424 μm pitch. Passing through the grid, the primary ionization

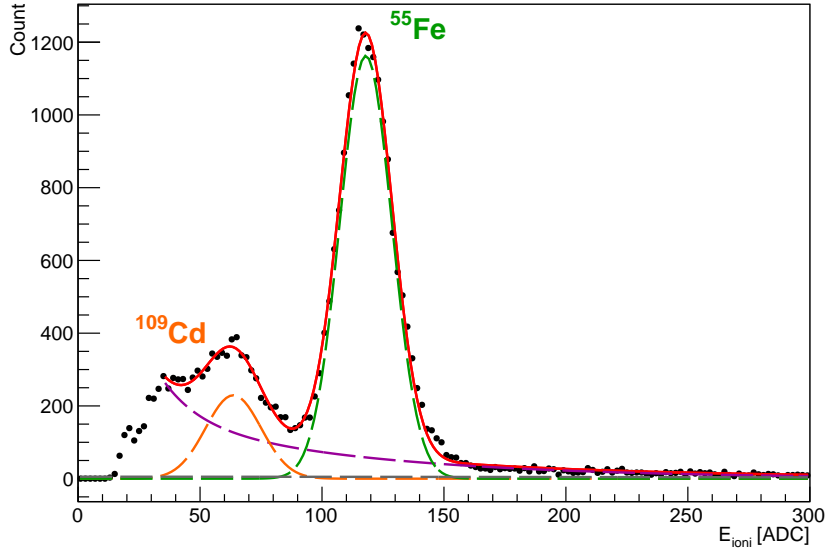


Figure 2: X-ray calibration spectrum measured with ^{109}Cd and ^{55}Fe sources. ^{109}Cd and ^{55}Fe sources produce X-rays at 3.04 and 5.96 keV respectively. The fit of the total spectrum is shown by the red-solid line showing the peak and background fits by dash lines.

electrons are amplified by avalanche in the 256 μm gap by a much higher electric field ($E_{\text{gain}} = 18.36 \text{ kV}\cdot\text{cm}^{-1}$). The pixelated micromegas is coupled to a fast self-triggered electronics (sampled at 50 MHz) specially developed for the MIMAC detector [17, 18]. The read-out composed of 512 channels, 256 channels covering the X-axis and 256 the Y-axis, allows the measurement of the ionization energy and the description of the envelope of the tracks of nuclear recoils with kinetic energies down to a few keV depending on the gas and pressure [14]. Each channel out of 512 has its own threshold determined by a calibration algorithm defining the intrinsic electronic noise level for each channel. In addition, the total ionization energy is measured by a charge preamplifier connected to the grid coupled to a flash-ADC sampled at the same frequency as the strip channels (50 MHz).

In order to prevent gain degradation due to the presence of impurities and O_2 , a closed circuit circulation gas system was implemented. The circulation system includes a buffer volume, an oxygen filter, a dry and very low leak pump ($3.8 \cdot 10^{-5} \text{ mbar}\cdot\text{L}/\text{s}$) and a pressure regulator. The gas is forced to circulate passing through the oxygen filter renewing the gas in the volume of the chamber every hour.

1.1.1 Ionization energy calibration

The detector calibration was performed by means of two X-rays radioactive sources: the ^{109}Cd and ^{55}Fe sources emitting X-rays respectively of 3.04 and 5.96 keV mean energies. Figure 2 shows the measured calibration spectrum. Two peaks can be identified which correspond to ^{109}Cd and ^{55}Fe sources on a continuum background. The continuum can be associated with Compton electrons and incomplete charge collection from the 22 keV

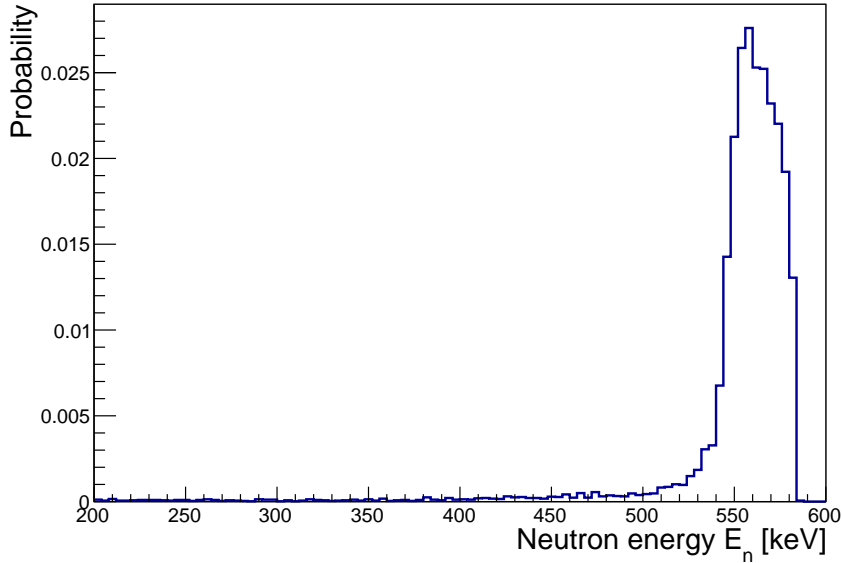


Figure 3: Left panel: simulation of the neutron spectrum interacting in the active volume of the detector placed at $D_{\text{target}} = 30$ cm and $\Theta = 0$. Neutron energies and direction distributions were estimated from the target using the TARGET software [19] and were propagated using MCNPX [21]

KX-ray of ^{109}Cd . This energy spectrum was fitted by the sum of two gaussian functions for the peaks and by the sum of two decreasing exponential functions for the continuum background. The MIMAC detector shows an energy resolution of 16 % at 3 keV. The radioactive sources have been hidden behind separated valves during the neutron detection.

1.2 MIMAC @ AMANDE facility

In general, as neutrons are the ultimate background for DM detection, these particles can be used for mimic a WIMP signal in DM detectors. In order to evaluate the MIMAC neutron detection response and its low energy electron/recoil discrimination, a mono-chamber MIMAC detector with an 18 cm drift space was placed in a monochromatic neutron field. It was generated by the AMANDE (Accelerator for Metrology And Neutron Applications for External Dosimetry) facility [20] at the IRSN of Cadarache by using a (p, n) nuclear reaction on a thin ^7Li target ($140 \mu\text{g}/\text{cm}^2$) on an AlF_3 backing.

This (p, n) nuclear reaction has many resonances one of them generating a neutron field with a maximum kinetic neutron energy of 565 keV at $\Theta = 0$. Here, Θ denotes the angle between neutron direction and the proton beam: kinetic energy of neutrons depends on Θ angle.

The MIMAC mono-chamber ($10 \times 10\text{cm}^3$) detector were placed at $\Theta = 0$ and at 30 cm distance. In this configuration, the solid angle covered by the detector is $\Omega = 0.111$ sr, thus neutron energy variations are small in the active volume and the neutron field can be considered as monochromatic, *i.e.* mono-energetic. In order to confirm this hypothesis,

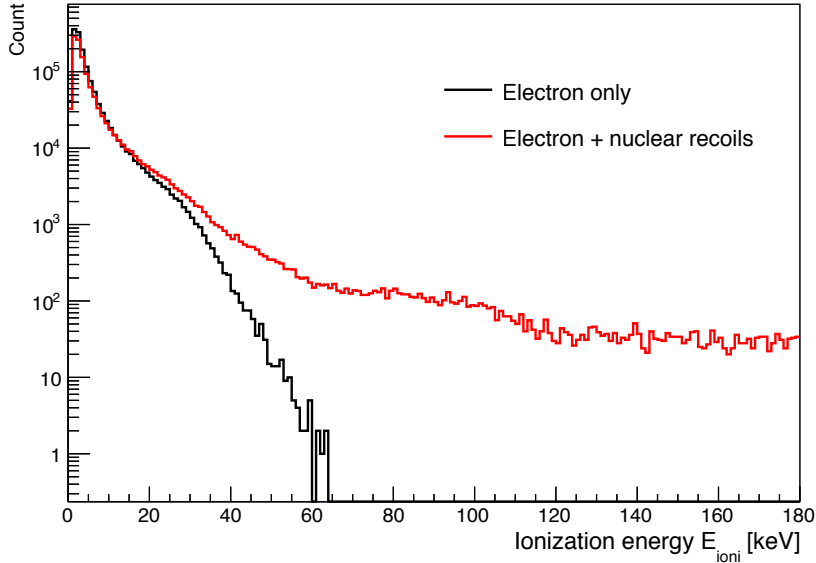


Figure 4: Raw MIMAC energy spectra measured at the AMANDE facility. The black line corresponds to the target without ${}^7\text{Li}$ (only electron events) and the red one to the target with the ${}^7\text{Li}$ (electron and nuclear recoil events).

a Monte-Carlo model of the neutron production and propagation was developed. Angular and energy distribution of neutrons outgoing from the target were estimated using TARGET software [19] and neutrons were propagated by Monte Carlo using MCNPX [21] considering the full geometry of the detector and the experimental hall. Figure 3 presents the Monte-Carlo simulation of the kinetic energy spectrum of neutrons interacting in the active volume showing the mean energy of the monochromatic neutron field produced at 565 keV with an energy resolution of $\Delta E_n/E_n = 3\%$. The tail of the distribution corresponds to the backscattered neutrons. In conclusion, the neutron field can be considered as a monochromatic neutron field.

In addition, neutron production is going along with an important γ -rays background from (p, γ) reaction on ${}^7\text{Li}$ and ${}^{19}\text{F}$. Indeed, proton bombardment of ${}^7\text{Li}$ and ${}^{19}\text{F}$ produces high energy γ -rays lines (from ~ 15 to ~ 18 MeV for ${}^7\text{Li}$ and from ~ 6 to ~ 7 MeV for ${}^{19}\text{F}$) in 4π [22]. The relative amplitude of these lines depends on the proton beam energy.

1.2.1 Fast neutron detection

Neutron elastic scatterings on nuclei in the active volume produce nuclear recoils with kinetic energies ranging from 0 to the maximum transferred kinetic energy depending on the nucleus mass, the so-called end-point. 565 keV neutrons transfer up to 107 keV in kinetic energy to ${}^{19}\text{F}$ recoils. However, for nuclear recoils there is a difference between the measurable ionization energy and the kinetic energy which is parametrized by the ionization quenching factor (IQF). This difference increase as the kinetic energy decreases. The IQF depends, in addition, on the nuclear recoil mass and gas properties (composition, pressure,

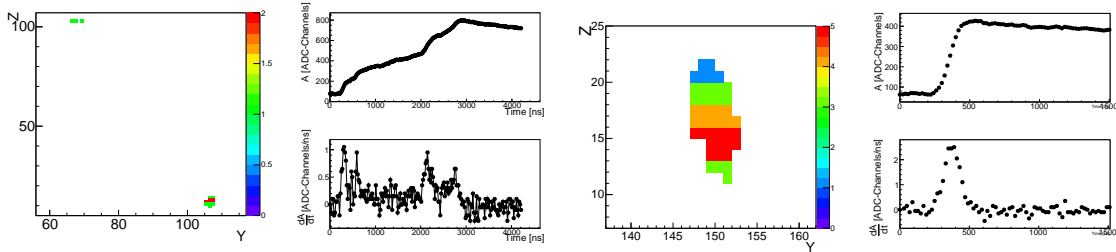


Figure 5: Left and right panels present respectively the (Y, Z) projection, the charge integrator amplitude and its first derivative of a 36.8 keV electron track and a 20.5 keV nuclear recoil track. The Z axis is in units of time-slices (20 ns each) and the Y axis in strip numbers. The colour scale corresponds to the relative number of strips fired in each time-slice.

temperature and impurities) and it can be estimated using the SRIM simulation code or measured as proposed in [23]. In the case of fluorine, taking into account an estimation of the IQF from our measurements [23], a 107 keV nuclear recoil should release in ionization roughly 57 keV.

The neutron production method using the ${}^7\text{Li}(p,n)$ nuclear reaction produces an important γ -ray background from (p, γ) channels on the Li target and on the fluorine of the AlF_3 backing. These γ -rays induced a huge number of electron recoils mainly by Compton scattering in the detector vessel, field cage and gas volume.

In order to evaluate the electron event rejection, data-taking with and without ${}^7\text{Li}$ on the target were performed. In the first case, we have a neutron production along with an important γ -ray production from the AlF_3 backing. In the second case, with only the AlF_3 backing, only γ -rays are produced. Figure 4 shows the raw energy spectra measured by the MIMAC chamber at the AMANDE facility with (red line) and without (black line) ${}^7\text{Li}$ on the target. Both spectra present quite the same shape below 30 keVee. On the " γ -rays only" spectrum (black line), we can see that the ionization energy released by electrons in the active volume does not exceed 60 keVee. This is due to the combined effects of detector geometry, the low electronic stopping power density and the long tracks of high energy electrons at 50 mbar. The raw " $n + \gamma$ -rays spectrum" shape makes even difficult to identify the two end-points from fluorine and carbon. The proton end-point at 565 keV is out of the Flash-ADC range.

2 Discriminating observables

The charge integrator amplitude is continuously read by the MIMAC electronic read-out. An event is acquired recording both strips of pixels and grid information only if the following condition is fulfilled:

$$A[i] - A[i - 16] > E_{th} \text{ (ADC units)} \quad (2.1)$$

where $A[i]$ is the preamplifier amplitude in the i^{st} 20 ns time-slice and E_{th} the threshold value. Figure 5 presents typical electron (left panel) and nuclear recoil (right panel) track

projections on the (Y, Z) plane associated to their preamplifier signals and its first derivative. This figure highlights the differences on the track topology and on their pulse-shape. The electron event (Y, Z) projection shows two small pixel clusters instead of the nuclear recoil event projection showing only one big cluster with a well-defined spatial development. The electronic event profile presents several "jumps" associated to charge clusters, while the nuclear recoil event presents only one "jump" with a faster rise-time.

For directional DM search, 3D tracks reconstruction of nuclear recoils [24] has to be performed to extract the track direction in the galactic rest frame. In order to get this 3D track determination, nuclear recoils have to be discriminated from electron and gamma background taking advantage of the electron and nuclear recoil event differences illustrated in Figure 5.

As a first step, to reject the active volume out(in)-going and miss reconstructed events some minimal cuts have to be applied. In a second step, an electron/recoil discrimination based on track topology and signal pulse-shape observables will be applied.

2.1 Minimal cuts

The minimal cuts applied to reject the mis-reconstructed events and out(in)-going events are the following:

Track. Primary electron ionization densities of electron tracks are often not sufficiently high to trigger the strips of pixels in one 20 ns time-slice. A first cut consists of requiring events with a 3D track *i.e.* more than one strip of pixels in coincidence (X and Y).

Out(in)-going events. We define an active volume on the (X, Y) projection to the anode in order to reject all out(in)-going events. For these events, only a part of their track is included in the active volume and the energy measurement will be misestimated.

Clustering. The ionization (electron-ion) pair distribution produced by a nuclear recoil is denser, per length unit, than the distribution produced by an electron of the same energy even taking into account the *IQF*. This is due to the fact that the total integrated stopping power of a nuclear recoil is higher than electron one at the same energy mainly from its much shorter track. We define a track cluster by a set of contiguous strips of pixels fired during a number of 20 ns time-slices. A nuclear recoil event will present only one cluster instead of the electron events presenting in general more than one. We will reject events presenting more than one cluster. Only those with two clusters separated in the X-Y projection by only one strip of pixels will be accepted.

Table 1 shows the impact of each minimal cut on the data sample used in the analysis. Track requirement is the dominant cut and we can note that this cut has a higher effect on the electron only sample (91% reduction) than on the nuclear recoil and electron sample(80% reduction). This difference comes from that the probability to fire the strip of pixels is lower for an electron than for a nuclear recoil. In order to apply the two remaining cuts, tracks are required. The application of the (X, Y) fiducialisation shows respectively a 1% and a 7% reduction of both samples. This difference comes from the fact that due to their ionization density, high energy electrons could not fire edge strips and cannot be identified as out/in-going event which is not the case for nuclear recoils. The 45% and 31% reduction coming from the application of the cluster cut has the same origin.

Cuts	Without Li	With Li
None	893779	795596
Track	78910	154603
Track + (X, Y) fiducialisation	77629	143855
Track + Cluster	43605	105978
Track + (X, Y) fiducialisation + Cluster	42979	99334

Table 1: Detail of the impact of minimal cuts combination on the number of events in the two sets of data: without and with Li target.

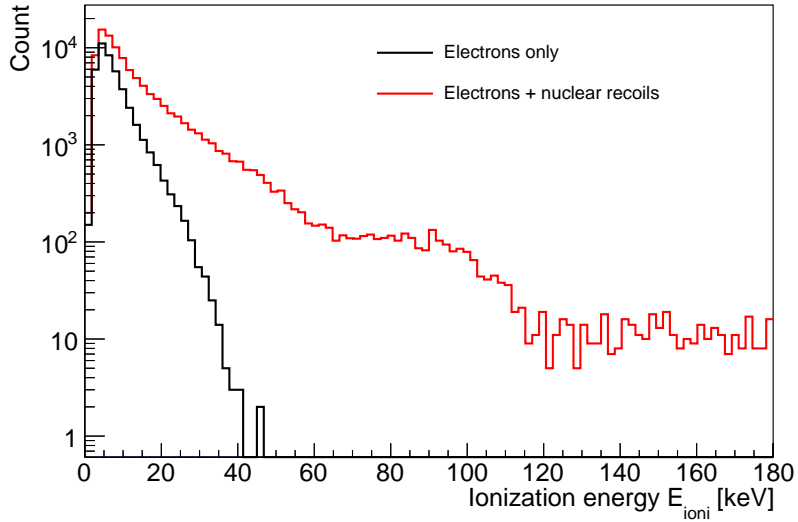


Figure 6: Total energy spectra obtained after the application of minimal cuts. The black line corresponds to events detected with the target without ${}^7\text{Li}$ (only γ -rays produced) and the red one to those detected with ${}^7\text{Li}$ on the target (γ -rays and neutrons produced).

Figure 6 shows the energy spectra measured by the MIMAC chamber at the AMANDE facility with (red line) and without (black line) ${}^7\text{Li}$ on the target. These spectra are obtained after the application of the minimal cuts described above. On the " $n + \gamma$ -rays" spectrum, ${}^{19}\text{F}$ and ${}^{12}\text{C}$ end-points at 57 and 110 keVee can clearly be identified. These end-points define the maximum kinetic energies affected by the *IQF*. In the case of ${}^{19}\text{F}$ the *IQF* was measured at 46% at 50 keV kinetic energy by the method proposed in [23], showing that the end point at 57 keV in ionization is consistent with our measurements. The ${}^1\text{H}$ end-point at 565 keV even affected by the quenching is out of range.

2.2 Discriminating observables

Using both, the charge preamplifier profile signal and the track topology, several observables are defined to discriminate nuclear recoil events from electron recoil ones. We can distin-

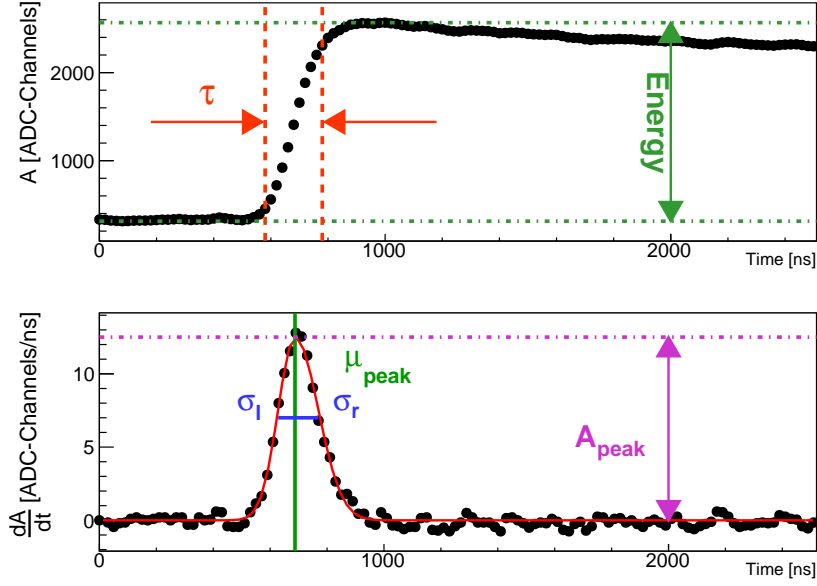


Figure 7: Top panel: A 38.3 keV event preamplifier amplitude as a function of time. The green arrow represents the ionization energy. The red arrows and dashed lines represent the rise-time definition. Bottom panel: The preamplifier amplitude first derivative as a function of time. The red line shows the fit with an asymmetric gaussian function. The purple, green and blue lines presents the fit parameters.

guish two kinds of observables: pulse-shape and track topology observables. Figures 8 and 9 present the one-dimension distribution for each observable. Black line corresponds to the events detected with the target without ${}^7\text{Li}$ (only γ -rays) and the red one to those detected with ${}^7\text{Li}$ (γ -rays and neutrons)

The pulse-shape is directly related to the primary electron-ion pairs distribution shape in the active volume. Using the fast pre-amplifier response (roughly 60 ns rise-time) several observables are defined. Figure 7 shows a 38.3 keV event preamplifier amplitude as a function of time and its first derivative illustrating some observable definitions.

Ionization Energy (E_{ioni}). The ionization energy is defined as the difference between the maximum and minimum preamplifier signal amplitudes. Top panel of figure 7, illustrates the energy measurement from a typical flash-ADC signal.

Offset ($A[0]$). As the anode is continuously read by the electronics, before triggering, an event could have a residual charge coming on the grid from an event that has not had enough charge to trigger the preamplifier. This residual charge coming before the event in the preamplifier is called the offset. In the case of an electron recoil, the ionization density along the z-axis could be not enough to trigger the charge preamplifier.

Preamplifier first derivative fit parameters (A_{peak} , $\Delta A_{\text{peak}}/A_{\text{peak}}$, μ_{peak} , $\Delta\mu_{\text{peak}}/\mu_{\text{peak}}$, σ_{peak} , $\log_{10}(\Delta\sigma_{\text{peak}}/\sigma_{\text{peak}})$, R_{peak} , γ_{peak}^1). The peak in the first derivative of the preamplifier signal is fitted using an asymmetric gaussian function (*i.e.* $\sigma_l(x < \mu) \neq \sigma_r(x > \mu)$). From this fit four parameters are extracted: the amplitude A_{peak} ,

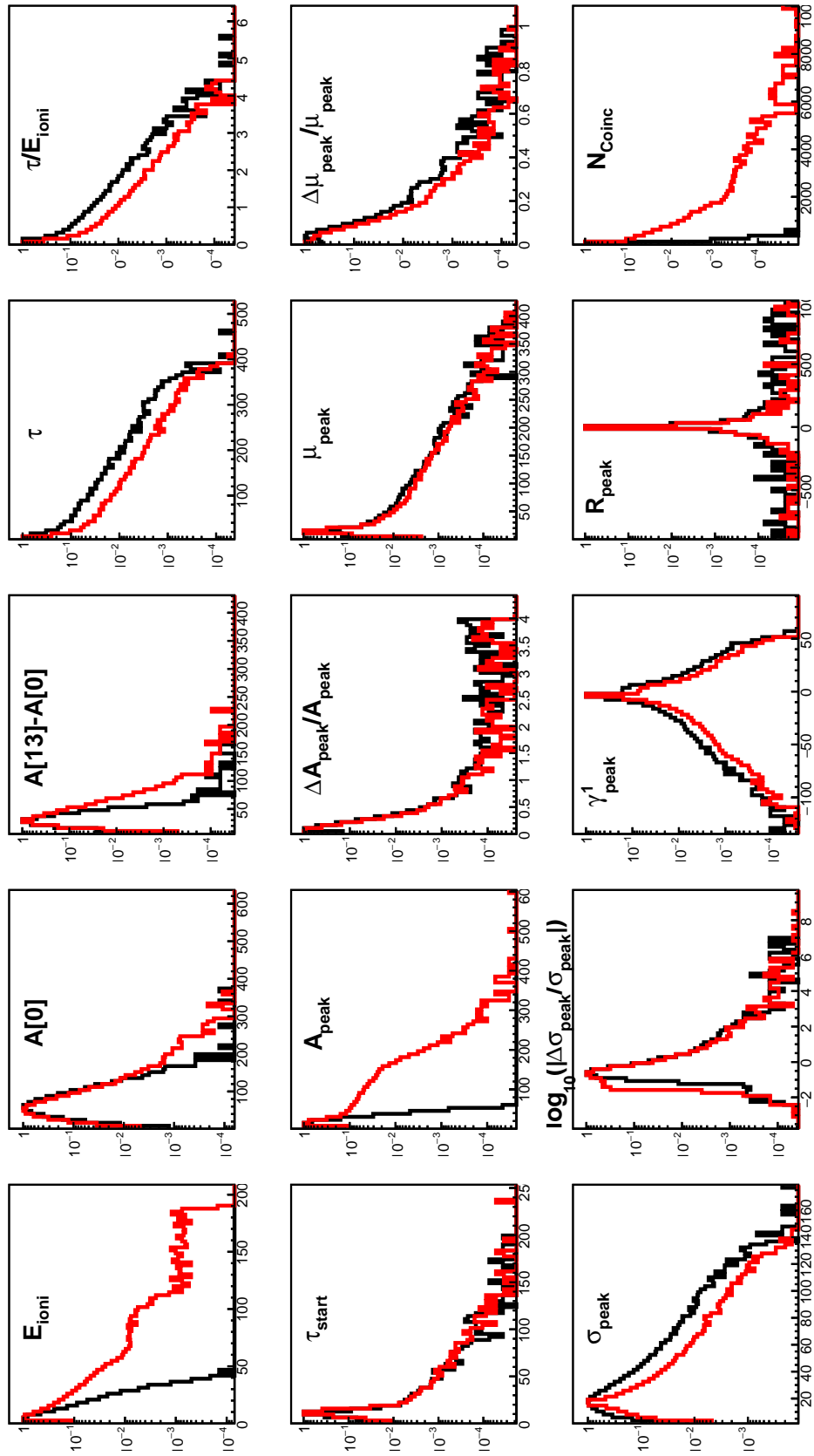


Figure 8: One-dimension distribution of each discriminating observables (part 1/2). The black line corresponds to the events detected with the target without ${}^7\text{Li}$ (only γ -rays) and the red one to those detected with ${}^7\text{Li}$ (γ -rays and neutrons).

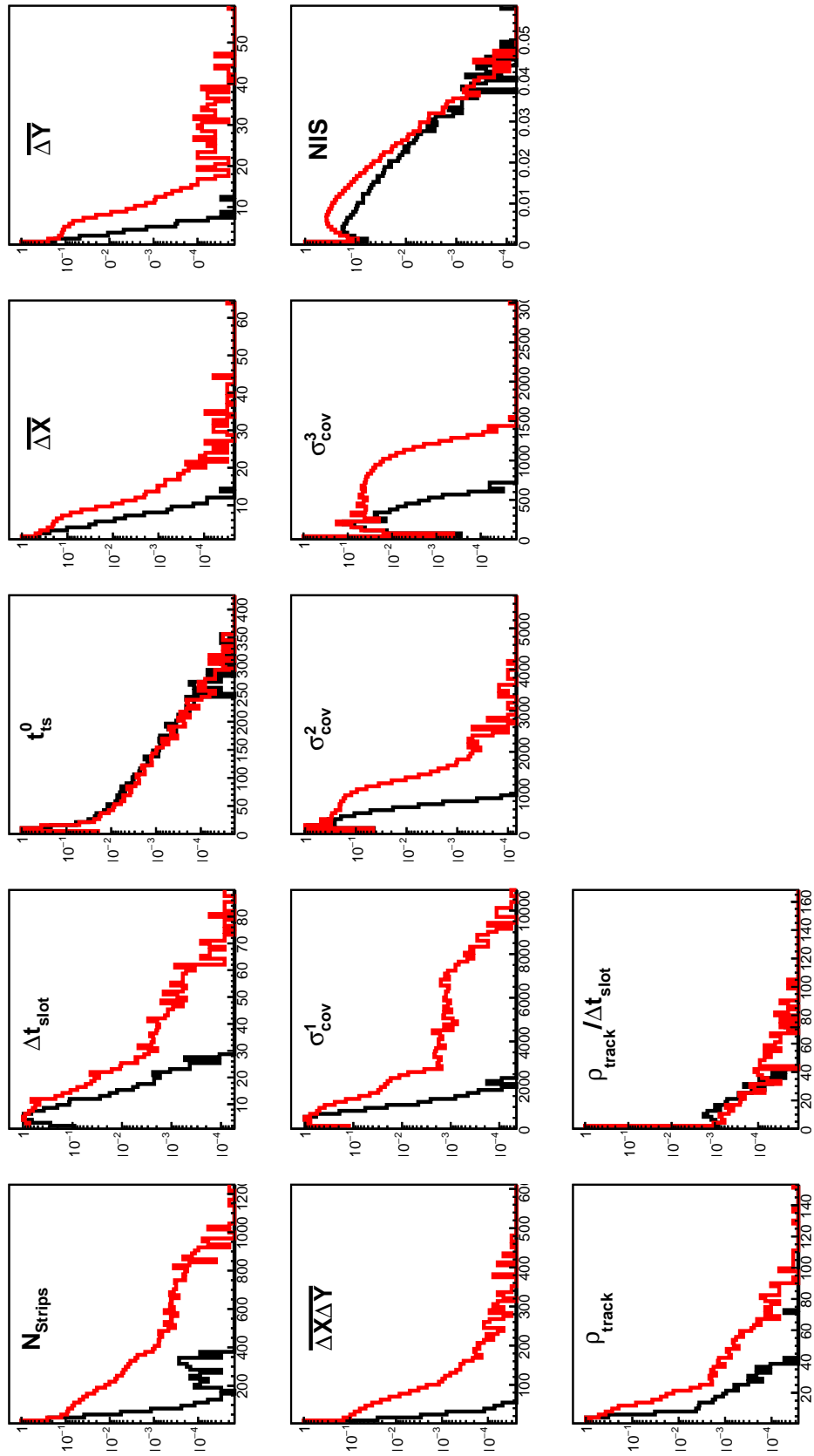


Figure 9: One-dimension distribution of each discriminating observables (part 2/2). The black line corresponds to the events detected with the target without ${}^7\text{Li}$ (only γ -rays) and the red one to those detected with ${}^7\text{Li}$ (γ -rays and neutrons).

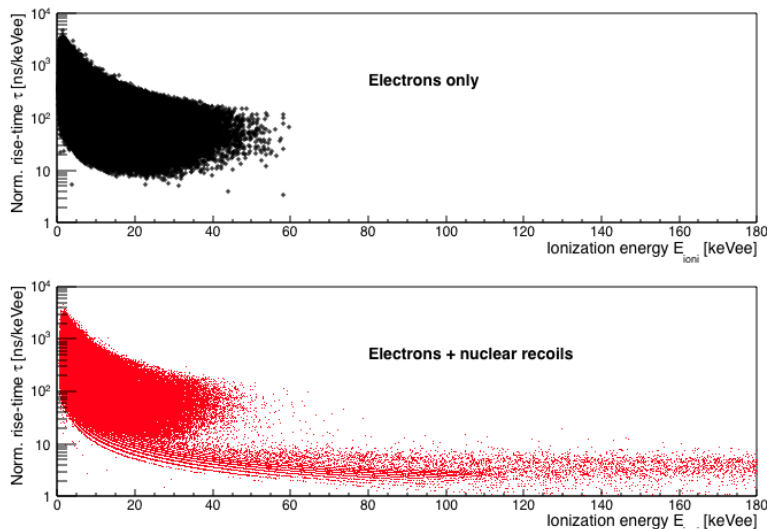


Figure 10: Event distributions on the plane $(E_{\text{ioni}}, \tau/E_{\text{ioni}})$. The black dots correspond to the events detected with the target without ${}^7\text{Li}$ (only γ -rays produced) and the red one to those detected with ${}^7\text{Li}$ on the target (γ -rays and neutrons produced)

the time position μ_{peak} , the left half-width σ_l and the right half-width σ_r . From the last two parameters, we can define an asymmetry factor $R_{\text{peak}} = \sigma_l/\sigma_r$ associated to the charge collection. In addition the reduced χ^2_{peak} is calculated.

Rise-Time and normalized Rise-Time (τ , τ_{start} and τ/E_{ioni}). The rise-time is defined as the time elapsed between 10 % and 90 % of the maximum amplitude of the preamplifier signal. This rise-time depends, obviously, on the event ionization energy. In order to define a discriminating observable, we normalize it by the total ionization energy τ/E_{ioni} . Figure 10 presents the event distributions in the $(E_{\text{ioni}}, \tau/E_{\text{ioni}})$ plane for $n + \gamma$ -rays (red dots) and γ -rays only (black crosses). This figure shows that the nuclear recoil normalized rise-time is systematically lower than the electron normalized rise-time. Moreover, we define the start rise-time τ_{start} as the time when the preamplifier amplitude is higher than 10 % of the maximum amplitude.

The pixelated Micromegas coupled to the fast electronics provide a sampling of the (X, Y) ionization electron density as a function of time. As previously mentioned, by knowing the electron drift velocity, a 3D track could be reconstructed. Figure 11 shows projections of a 38.8 keVee track on (X, Z) , (Y, Z) , (X, Y) planes and its 3D reconstruction. In this figure, the graphic representation of ΔX_i , the width of the i^{st} time-slice along the x axis, is also shown. Then, using this information, we define a set of track observables which some of them are illustrated in figure 11.

Track duration and track start (Δt_{slot} and t_{track}^0). Figure 11 illustrates the definition of the track duration Δt_{slot} . The track duration is the difference between the last time-slice ($t_{\text{track}}^{\text{end}}$) and the first one (t_{track}^0) as shown in figure 11. This observable is related to the projection of the track length along the z -axis. On the other hand, t_{track}^0 is the time-slice number of the first strip coincidence. The shift between the trigger and t_{track}^0

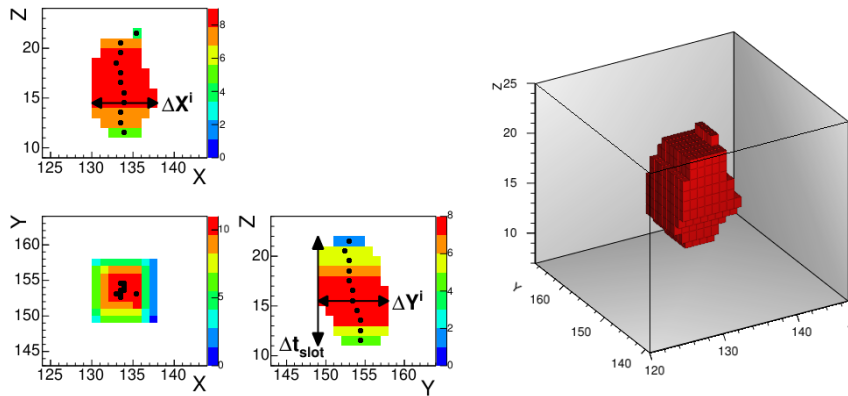


Figure 11: Right panels: projections of a 38.3 keVee nuclear recoil track in the (X, Z) , (Y, Z) and (X, Y) plans. The Z axis is in units of time-spice (20 ns) and the X axis in strip number. The black dots represent the time-slice barycenter position. The vertical arrow represents the definition of the track duration. The horizontal arrow represents one time-slice width ΔX along the X axis. The colour scale corresponds to the relative number of strips fired in the time-slice.

is related to the ionization electron density. In the case of an electron recoil, the value of t_{track}^0 may fluctuate due to the low ionization density. In contrast, in the case of nuclear recoils this shift is expected to be more or less constant.

Strip and coincidence number N_{strips} and N_{coinc} . The strip number and coincidence number correspond respectively to the total number of strips and (X, Y) coincidences triggered during the event. If the full primary electron ionization density is detected, these two quantities are expected to be linearly correlated. Nuclear recoil ionization density is sufficiently important to trigger strips and (X, Y) coincidence in one 20 ns time-slice, whereas for electron recoils this is not the case.

Normalized Integrated Straggling (NIS). The NIS is defined as the sum of each barycenter deviation $\Delta\theta_i$ along the track and normalized by the ionization energy:

$$NIS = \frac{1}{E_{ioni}} \sum_{i=1}^{N_s-2} \Delta\theta_i \quad (2.2)$$

This observable estimates the integrated straggling along the track. The straggling depends on the recoil mass and gas pressure. The NIS of the electrons will be larger than the NIS of nuclear recoils of the same kinetic energy [13].

Track density and normalized track density (ρ_{track} and $\rho_{track}/\Delta t_{slot}$). This observable is related to the primary ionization electron density. It is defined as:

$$\rho_{track} = \sum_{i=1}^{N_s} \frac{N_{pix}^i}{\Delta X^i \times \Delta Y^i} \quad (2.3)$$

where N_s is the number of time-slices, N_{pix}^i is the number of pixels fired in the i^{st} time-slice and $\Delta X(Y)^i$ the width on the $X(Y)$ axis in the i^{st} time-slice. The nuclear recoil track

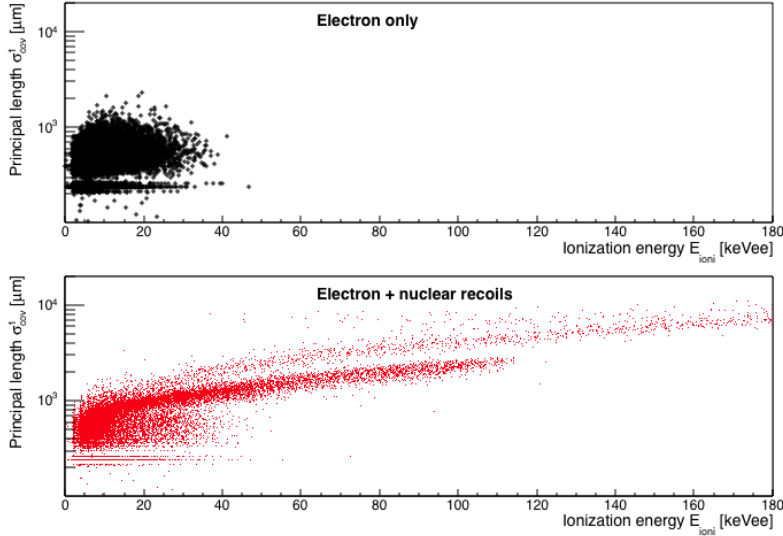


Figure 12: Event distributions on the plane $(E_{\text{ioni}}, \sigma_{\text{cov}}^1)$. The black dots correspond to the events detected with the target without ${}^7\text{Li}$ (only γ -rays) and the red ones to those detected with ${}^7\text{Li}$ (γ -rays and neutrons) on the target.

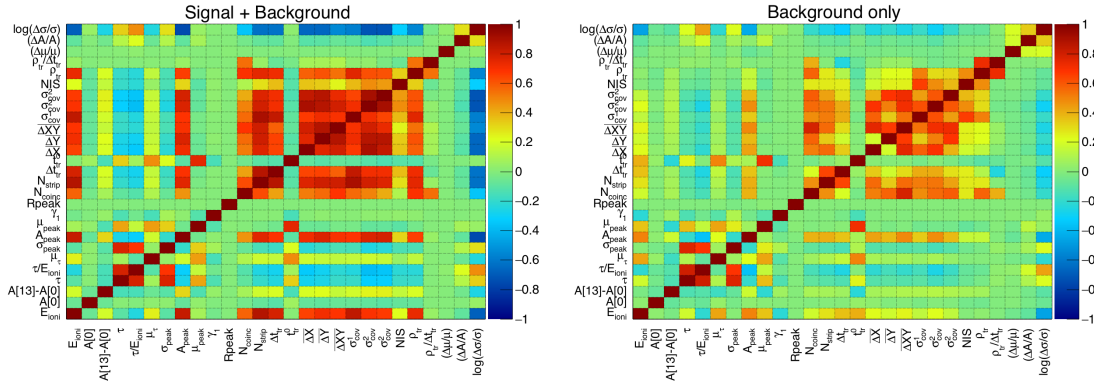


Figure 13: The left and right panels present the correlation matrices of the MIMAC observables used for the Boosted Decision Tree (BDT) analysis. The left panel corresponds to the measurement with the ${}^7\text{Li}$ (γ -rays and neutrons) and the right panel to the measurement without ${}^7\text{Li}$ (only γ -rays).

density will be, in general, higher than the electron track density due to the number of "holes" present in an electron track, see figure 11. Moreover, we defined the normalized track density as $\rho_{\text{track}}/\Delta t_{\text{slot}}$.

Track widths ($\overline{\Delta X}$, $\overline{\Delta Y}$ and $\overline{\Delta X \Delta Y}$). From the $\Delta(X/Y)^i$ time-slice width, we calculate the mean of ΔX , ΔY and $\Delta X \Delta Y$. Mean value of ΔX and ΔY are related to the track length projected along the X and Y axis. In the cas of tracks almost contained in the (X, Y) plane, these observables are sensitive to the track length: in comparison with a nuclear recoil, lower value of $\overline{\Delta X}$ and $\overline{\Delta Y}$ are expected for an electron recoil. The

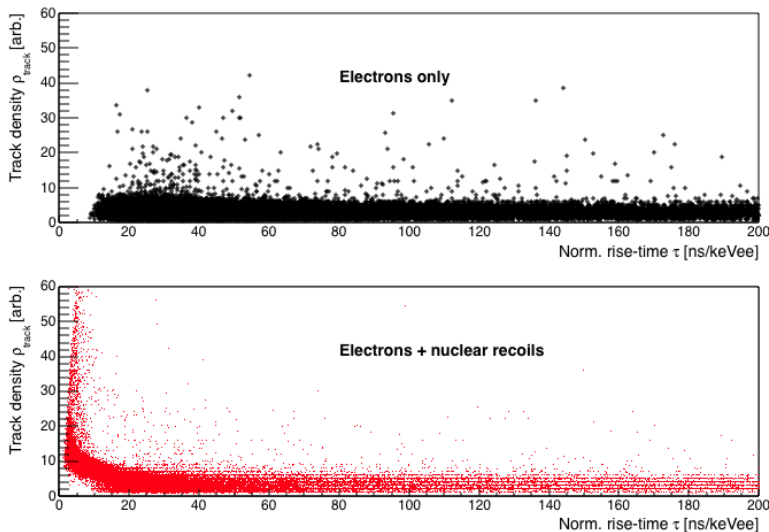


Figure 14: Event distributions on the plans $(\tau/E, \rho_{\text{track}})$. The black dots correspond to the events detected with the target without ${}^7\text{Li}$ (only γ -rays) and the red ones to those detected with ${}^7\text{Li}$ (γ -rays and neutrons) on the target.

$\overline{\Delta X \Delta Y}$ observable corresponds to the mean surface of the track on the anode plane, the same behavior is expected for this observable.

Track principal component length and widths ($\sigma_{cov}^1, \sigma_{cov}^2$ and σ_{cov}^3). As shown in the right panel of figure 11 we can reconstruct a 3D track from the MIMAC read-out. From this information and using a principal component analysis, we can calculate the longitudinal track length σ_{cov}^1 and its transverse widths σ_{cov}^2 and σ_{cov}^3 . These lengths are the eigenvalues of the track position covariance matrix. The longitudinal track length observable σ_{Long} is another estimator of the track length. These observables are related to the electron diffusion in the drift space and to the track direction. Indeed, for a nuclear recoil event an X/Y asymmetry is expected from the track direction. However, this track "fitting" approach is not adapted for direction extraction for low energy recoils ($E_{ioni} < 40$ keV). A more complex method is needed in order to determine the track direction with the MIMAC read-out. A dedicated paper [24] has proposed an original likelihood method based on track simulations for low energy tracks.

Figure 12 represents the event distributions in the $(E_{ioni}, \sigma_{cov}^1)$ plan for $n + \gamma$ -rays (red dots) and γ -rays only (black crosses). Two different regions corresponding to electrons and nuclear recoils can be identified. Moreover, on the $n + \gamma$ -rays distribution two branches can be identified, corresponding the shorter one to fluorine and carbon recoils and the longer one to proton recoils.

Figure 13 shows the correlation matrices of the observables defined above for the $n + \gamma$ -rays (left panel) and γ -rays only (right panel) samples. These correlation matrices illustrate the previous observation. Indeed, in the $n + \gamma$ -rays sample, the ρ_{track} and τ/E observables are anti-correlated (-25%) while in the γ -rays only sample, these observables are almost uncorrelated (-3%). Figure 14 shows the event distributions in the $(\tau/E, \rho_{\text{track}})$ plan for

$n + \gamma$ -rays (red dots) and γ -rays only (black crosses), illustrating the previous correlation values. We can clearly identify two different regions corresponding to electron and nuclear recoils. This figure illustrates the electron/recoil separation and the complementary of flash (τ/E) and track (ρ_{track}) observables. Moreover, N_{Coinc} is correlated at 33 % with the normalized track density ($\rho_{track}/\Delta t_{slot}$) for the $n + \gamma$ -rays sample and it is anti-correlated at -27 % for the γ -rays only sample. These two examples illustrate how the observable combination will be used to differentiate both samples.

3 Electron/recoil discrimination by boosted decision trees

As demonstrated in [13], a sequential analysis of the electron/recoil discrimination is not sufficient to get a good discrimination power ($10^4 - 10^5$). In this section, a boosted decision trees (BDT) analysis strategy and the results obtained will be presented.

3.1 Boosted decision trees analysis strategy

Boosted decision trees [25] is a multivariate analysis algorithm widely used in high-energy physics. It can be seen as a data classifier, often employed for signal/background discrimination. It is based on the optimization of successive linear cuts on different discriminant observables. The classification given by the BDT analysis is encoded on a BDT response variable defined as:

$$X_{\text{BDT}} = \sum_{i=1}^{N_{\text{trees}}} \alpha_i T_i(\tilde{\mathcal{O}}) \quad (3.1)$$

where N_{trees} is the number of trees used for boosting, α_i the normalized weight of each tree T_i and $\tilde{\mathcal{O}}$ the observables used in the analysis. By definition, the BDT variable value must be between -1 and 1.

In the particular case of the electron/recoil discrimination, the two following hypotheses are tested for each event:

$$\begin{cases} H_0 = \text{electron } (e^-) \\ H_1 = \text{nuclear recoil } (R) \end{cases}$$

Using the data acquired with the fast neutrons produced at the AMANDE facility, it is not possible to obtain pure electron and/or nuclear recoil samples. The BDT analysis will be used to identify electron recoils on the nuclear recoil and electron sample by testing the two following hypothesis:

$$\begin{cases} H'_0 = \text{electron only } (i.e. \text{ without } ^7\text{Li}) \\ H'_1 = \text{nuclear recoil + electron } (i.e. \text{ with } ^7\text{Li}) \end{cases}$$

In conclusion, the BDT will be trained on AMANDE data set in order to separate electron recoils from the full data set acquired with ^7Li target.

We applied a BDT analysis by using the TMVA software framework [26]. We trained a forest of 2000 trees with 3.8×10^4 events. In order to avoid the over-training while maximizing BDT performances, we requested for each foil a minimum of 10% $\equiv 3.8 \times 10^3$ events and a maximal tree-level of 3. In order to evaluate the overtraining, we compared

Rank	Variable	Importance	Type
1	A_{peak}	8.718e-02	Pulse-shape
2	N_{Coinc}	7.662e-02	Track
3	$\rho_{track}/\Delta t_{slot}$	7.377e-02	Track
4	Δt_{slot}	7.157e-02	Track
5	N_{Strips}	7.026e-02	Track
6	t_{tr}^0	6.207e-02	Track
7	E_{ioni}	4.464e-02	Pulse-shape
8	τ	4.395e-02	Pulse-shape
9	μ_{peak}	4.352e-02	Pulse-shape
10	$A[0]$	3.620e-02	Pulse-shape
11	σ_{cov}^3	3.593e-02	Track
12	τ/E_{ioni}	3.563e-02	Pulse-shape
13	$A[13] - A[0]$	3.345e-02	Pulse-shape
14	σ_{peak}	3.254e-02	Pulse-shape
15	σ_{cov}^2	2.955e-02	Track
16	$\overline{\Delta Y}$	2.909e-02	Track
17	σ_{cov}^1	2.779e-02	Track
18	ρ_{track}	2.671e-02	Track
19	$\overline{\Delta X}$	2.542e-02	Track
20	$\log_{10}(\Delta\sigma_{peak}/\sigma_{peak})$	2.377e-02	Pulse-shape
21	τ_{start}	2.302e-02	Pulse-shape
22	$\Delta A_{peak}/A_{peak}$	1.948e-02	Pulse-shape
23	NIS	1.932e-02	Track
24	γ_{peak}^1	1.683e-02	Pulse-shape
25	$\overline{\Delta X \Delta Y}$	1.086e-02	Track
26	R_{peak}	8.228e-04	Pulse-shape
27	$\Delta\mu_{peak}/\mu_{peak}$	0.000e+00	Pulse-shape

Table 2: BDT ranking of the twenty-seven discriminant observables of the Boosted Decision Tree analysis with their associated importance (see text for definition).

the train and the test samples using the Kolmogorov-Smirnov statistic test. It tests if the train and the test samples follow the same probability distribution evaluating the maximal distance between the sample cumulative distributions. We measure a $D = 3.11 \times 10^3$ maximal distance corresponding to a 0.996 p-value. The confidence interval at 1σ is $[0; 4.9 \times 10^{-3}]$, it includes the maximal distance value. We can conclude that both samples follow the same probability distribution, validating our statement that our BDT analysis is not overtrained.

The table 2 presents the BDT ranking of the seventeen discriminant observables. The ranking was established by calculating the importance of each variable [26]. The importance is evaluated as the total separation-gain weighted by the number of events for each variable.

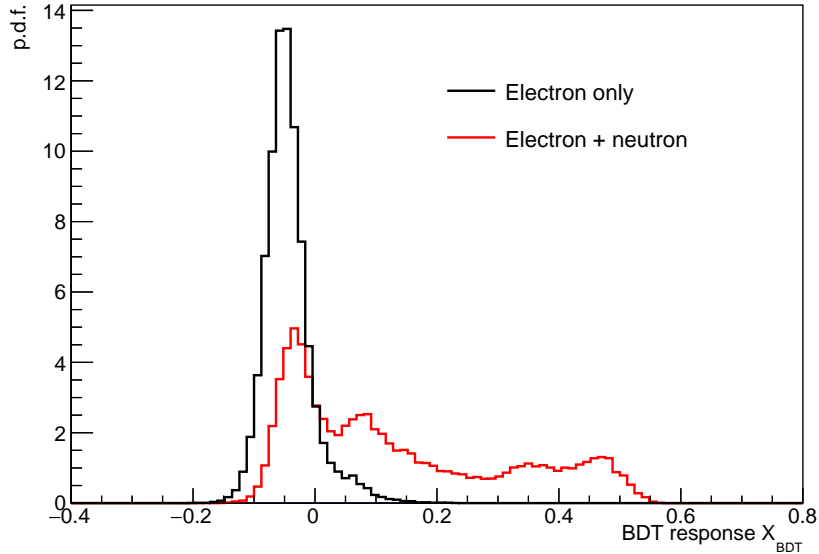


Figure 15: X_{BDT} value distribution for electrons only sample (black line) and for the electron and nuclear recoil sample (red line).

It quantifies the importance of an observable in a BDT analysis. This table shows that there is no dominant observable involved in the separation and it illustrates the complementarity of the pulse-shape and the 3D track observables for electron/recoil discrimination.

3.2 BDT analysis results

Figure 15 shows the X_{BDT} distribution from BDT analysis for each hypothesis (H'_0 and H'_1). Black and red lines correspond respectively to the X_{BDT} distribution for the electron only sample (without ${}^7\text{Li}$) and for the electron and nuclear recoil sample (with ${}^7\text{Li}$). The electron only sample presents a slightly asymmetric peak centered at -0.04 with its X_{BDT} value ranging from -0.2 to 0.2. The nuclear recoil and electron sample present the same structure as observed previously for X_{BDT} value lower than 0, showing that our analysis classify some events as electron recoils in the sample (with ${}^7\text{Li}$).

The rejection power of a cut on the X_{BDT} value is defined as the ratio between the total electron event number N_{elec} and the number of selected electron event N_{elec}^{sel} :

$$\xi_R = \frac{N_{elec}}{N_{elec}^{sel}} \quad (3.2)$$

This number corresponds to the size of the sample needed to have only one electron event passing the cut on the X_{BDT} value. It quantifies the goodness of the cut. From the distribution of $f(X_{BDT}|H_0)$ as shown by figure 15 (black line), it is possible to determine the value of a cut on X_{BDT} associated with a certain rejection power. Table 3 represents the value of the cut on X_{BDT} for rejection power ranging from 10^2 to 10^5 . The impact of these cuts on the experimental data is shown by figure 16. The left and right panels show

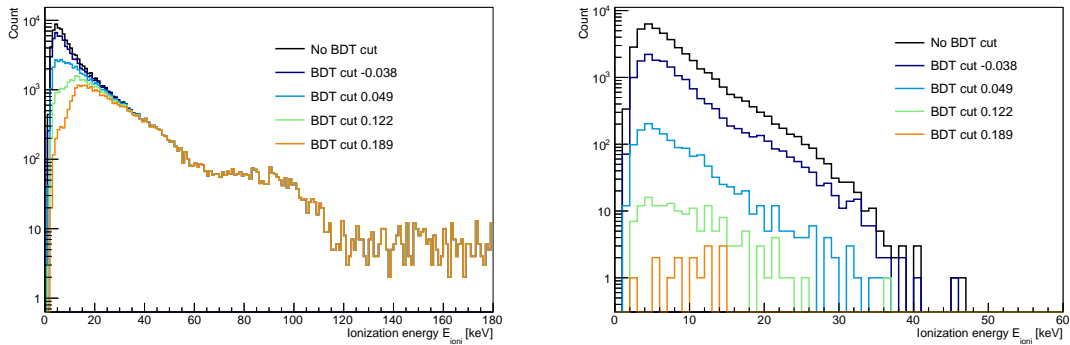


Figure 16: Energy spectra (left panel: with ${}^7\text{Li}$ (electron and nuclear recoil), right panel: without ${}^7\text{Li}$ (electrons only) obtained after the application of cuts on the X_{BDT} value as listed in table 3. Black lines represent energy spectra obtained without X_{BDT} cut.

Rejection power ξ_R	BDT cut X_{BDT}^{cut}
10^2	-0.038
10^3	0.049
10^4	0.122
10^5	0.188

Table 3: Association of rejection power ξ_R with cuts on X_{BDT} value obtained from X_{BDT} value distribution for electron recoil sample presented in figure 15.

respectively measured energy spectra with and without ${}^7\text{Li}$ target after the application of table 3 cuts. Right panel of figure 16 shows that as X_{BDT} cut increases, the high energy contribution (above 15 keV) to the electron energy spectrum is reduced. This effect is also visible on the left panel of figure 16: we can observe that a low energy contribution (below 20 keV) to the energy spectrum coming from electron is suppressed.

In conclusion, we showed that crossing all the MIMAC observables in a BDT analysis, we are able to reach a 10^5 rejection power level in the whole energy range.

4 BDT Analysis efficiency estimation

For rare event searches, it is essential to estimate the analysis efficiency which takes place in WIMP-nucleus scattering event rate estimation. It quantifies the probability for a nuclear recoil to be identified as a nuclear recoil. In order to estimate this quantity, as the sample of nuclear recoils is a mixed sample containing electrons, we develop a Monte-Carlo simulation of fluorine nuclear recoil detection by the MIMAC detector.

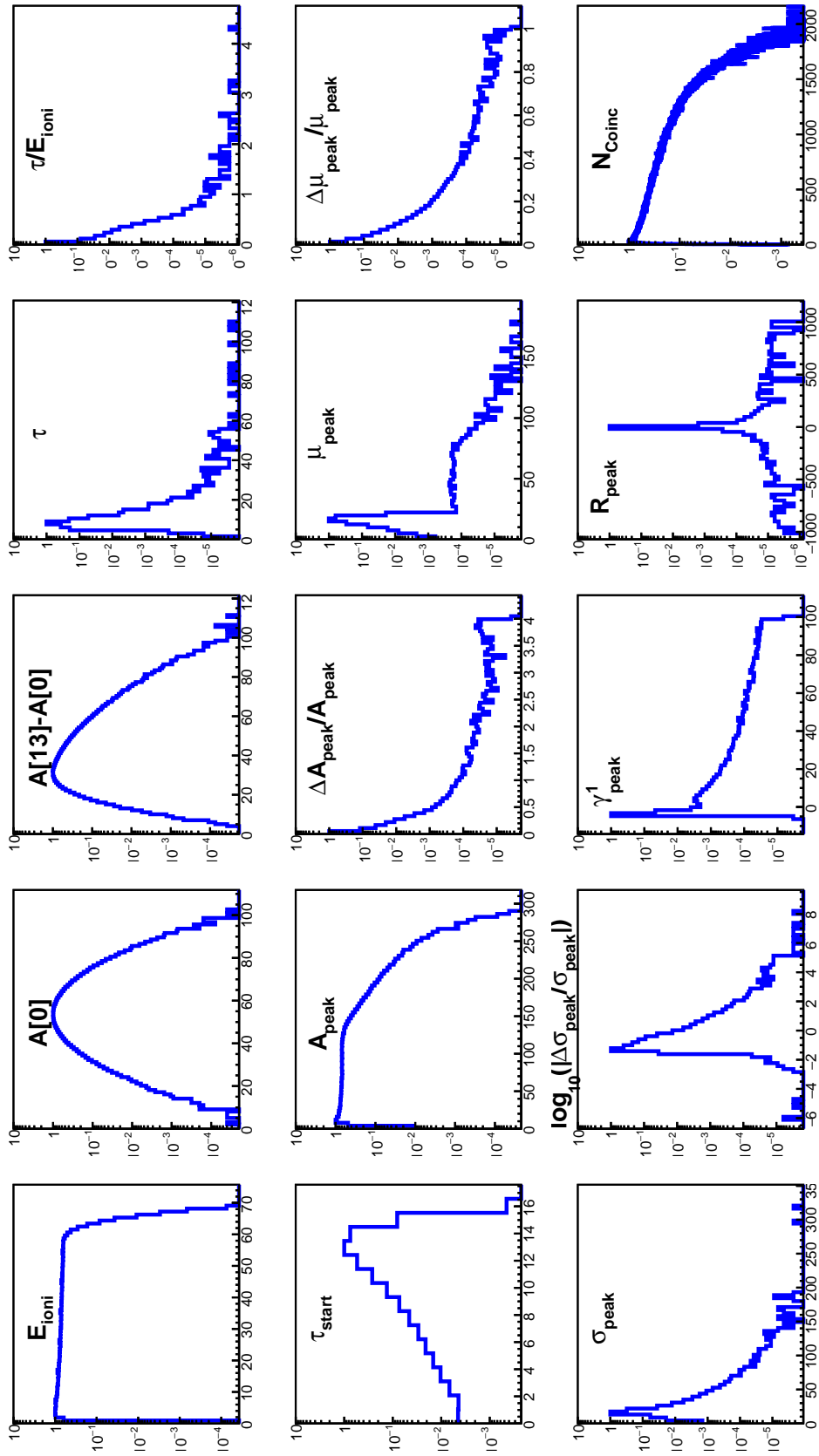


Figure 17: One-dimension distribution of each discriminating observables obtained from Monte Carlo for fluorine nuclear recoils (part 1/2). Only events triggering the detector and passing minimal cuts are represented.

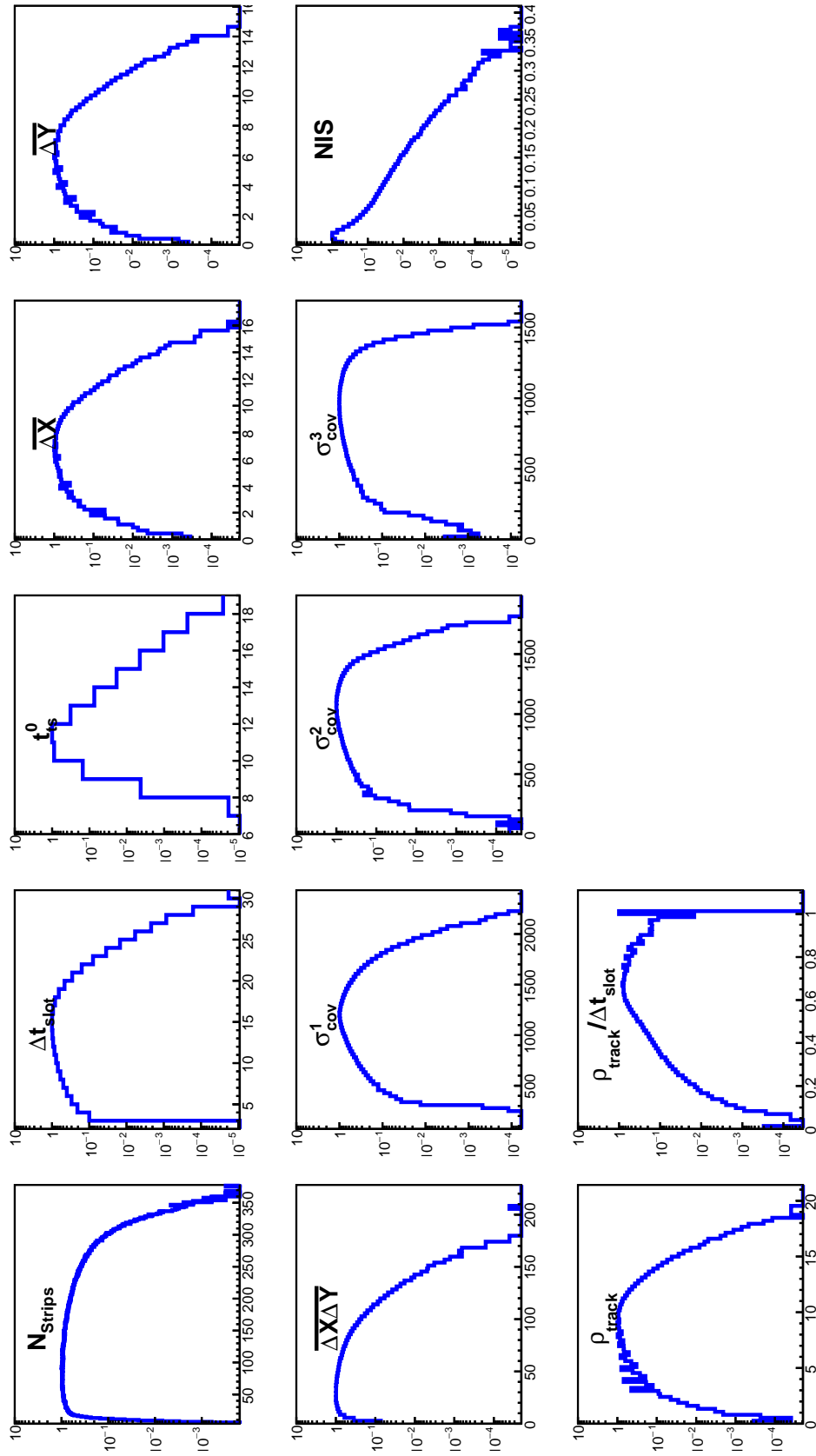


Figure 18: One-dimension distribution of each discriminating observables obtained from Monte Carlo for fluorine nuclear recoils (part 2/2). Only events triggering the detector and passing minimal cuts are represented.

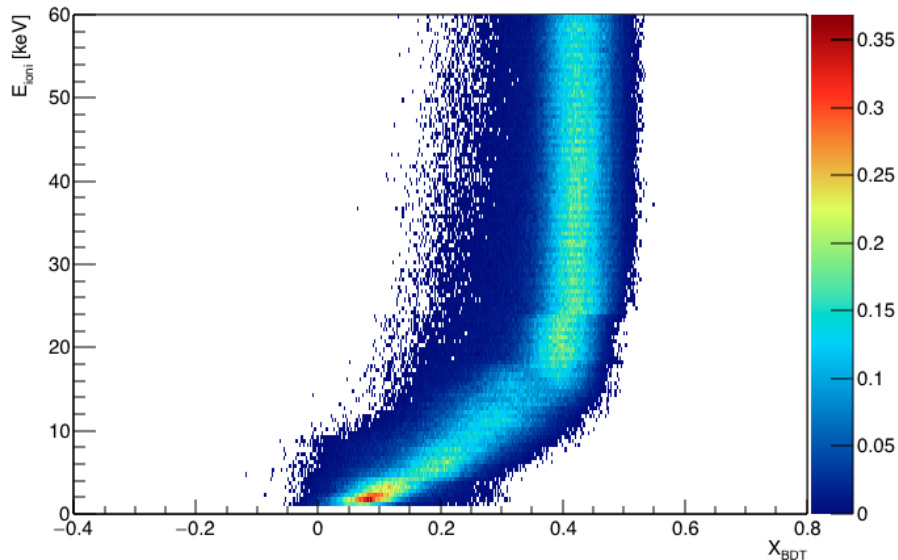


Figure 19: Fluorine event probability density function on the plane (X_{BDT}, E_{ioni}) estimated from Monte Carlo. The BDT classification previously obtained was applied to Monte-Carlo events generated as described in section 4.1.

4.1 Fluorine nuclear recoil simulation

In order to estimate the primary ionization electron distribution along tracks of fluorine nuclear recoils we used the SRIM software. 6.9×10^6 fluorine nuclear recoils were simulated with energies ranging from 1 to 100 keV in the MIMAC gas mixture at 50 mbar. Each track was randomly distributed in 4π in the whole active volume to scan every possible direction of nuclear recoils in dark matter search data. Taking into account the electron drift velocity and the transverse and longitudinal diffusion coefficients, estimated by Magboltz [27], we estimated the ionization electron distribution in the anode plan as a function of time. Then, using the micromegas geometry and the flash-ADC transfer function, we were able to model MIMAC raw data. Finally, using the observable reconstruction software, we obtained the observable distribution for a set of fluorine nuclear recoils as presented in figures 17 and 18. We can see that our Monte-Carlo simulation is able to reproduce the different observables for fluorine recoils.

4.2 BDT analysis efficiency estimation

The BDT classification, obtained previously, was applied on the simulated fluorine nuclear recoils. Figure 19 presents the probability density function of generated Monte-Carlo events in the plane (X_{BDT}, E_{ioni}) . We can note that the X_{BDT} value increases as the ionization energy increases.

The efficiency of a BDT cut is defined as the ratio of the number of nuclear recoils

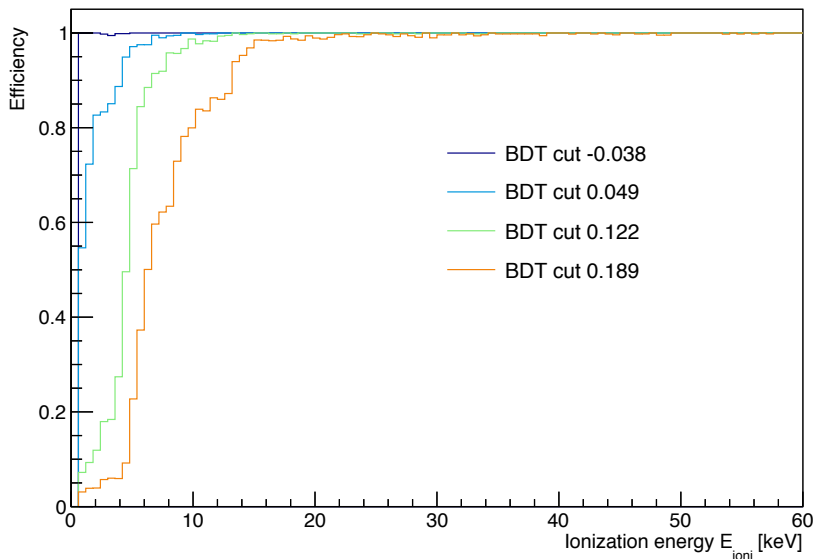


Figure 20: Analysis efficiency as a function of the ionization energy for several X_{BDT} cut values as listed in table 3.

passing the cuts N_{NR}^{sel} and the total number of nuclear recoils N_{NR} :

$$E = \frac{N_{NR}^{sel}}{N_{NR}} \quad (4.1)$$

Table 4 lists the analysis efficiency for each cut listed in table 3 considering the full energy range and several thresholds. The uncertainty on efficiency is obtained by error propagation assuming that N_{NR}^{sel} and N_{NR} follow a Poisson statistics. The study of the impact of the systematics on the efficiency request a complete study and will be the subject of an ongoing publication. We can note that a 10^5 electron rejection power is reached with a $86.49 \pm 0.17\%$ nuclear recoil efficiency considering the full energy range and $94.67 \pm 0.19\%$ and $98.83 \pm 0.21\%$ if we assume a 5 keV and 10 keV thresholds respectively.

Moreover, figure 20 represents the BDT analysis efficiency as a function of the ionization energy for several X_{BDT} cuts listed in table 3. For each X_{BDT} cut, we can see that the efficiency increases up to reach 100% as the ionization energy increases. In the case of a 10^5 rejection power cut, we obtained a 50% efficiency at 5 keV ionization energy with the present gain of the detector. This gain can be increased, if wished, to explore even better the low-energy range.

5 Conclusion

In this paper, we proposed an original method for electron event rejection based on a multivariate analysis applied to experimental data acquired using monochromatic neutron fields. This analysis shows that a 10^5 rejection power is reachable for electron/recoil discrimination

Rejection power ξ_R	X_{BDT} cut	Full range efficiency [%]	Efficiency with a lower threshold [%]	
			5 keV	10 keV
10^2	-0.038	99.77 ± 0.19	99.88 ± 0.20	99.93 ± 0.21
10^3	0.049	98.69 ± 0.19	99.74 ± 0.20	99.92 ± 0.21
10^4	0.122	92.94 ± 0.18	98.70 ± 0.20	99.81 ± 0.21
10^5	0.188	86.49 ± 0.17	94.67 ± 0.19	98.83 ± 0.21

Table 4: Association of rejection power ξ_R with cuts on X_{BDT} value and the corresponding total simulated efficiency. The efficiency is obtained from Monte-Carlo model described in section 4.1 and it is given for the full energy range and assuming a 5 keV and 10 keV thresholds. The given uncertainties only come from propagation of statistical uncertainty assuming a Poisson statistics.

in the ionization energy range. Moreover, the analysis efficiency was estimated showing that a 10^5 electron rejection power is reached with a $86.49 \pm 0.17\%$ nuclear recoil efficiency considering the full energy range and $94.67 \pm 0.19\%$ considering a 5 keV lower threshold. The efficiency uncertainty does not take into account systematic uncertainties of the detector.

Acknowledgements

We would like to thank M. Pepino and A. Martin for operating the AMANDE facility during the many experiments performed. We acknowledge F. Mayet for many helpful discussions. The MIMAC collaboration acknowledges the ANR-07-BLAN-0255-03 funding.

References

- [1] D. S. Akerib, H. M. Araújo, X. Bai et al., *First Results from the LUX Dark Matter Experiment at the Sanford Underground Research Facility*, *Phys. Rev. Lett.* **112** (Mar., 2014) 091303, [[arXiv:1310.8214](#)].
- [2] E. Aprile, M. Alfonsi, K. Arisaka et al., *Dark Matter Results from 225 Live Days of XENON100 Data*, *Phys. Rev. Lett.* **109** (Nov., 2012) 181301, [[arXiv:1207.5988](#)].
- [3] E. Aprile, M. Alfonsi, K. Arisaka et al., *Limits on Spin-Dependent WIMP-Nucleon Cross Sections from 225 Live Days of XENON100 Data*, *Phys. Rev. Lett.* **111** (July, 2013) 021301, [[arXiv:1301.6620](#)].
- [4] DARKSIDE collaboration, P. Agnes et al., *Low Radioactivity Argon Dark Matter Search Results from the DarkSide-50 Experiment*, [[arXiv:1510.00702](#)].
- [5] E. Armengaud, C. Augier, A. Benoît et al., *Search for low-mass WIMPs with EDELWEISS-II heat-and-ionization detectors*, *Phys. Rev. D* **86** (Sept., 2012) 051701, [[arXiv:1207.1815](#)].
- [6] R. Agnese, A. J. Anderson, M. Asai et al., *Search for Low-Mass Weakly Interacting Massive Particles Using Voltage-Assisted Calorimetric Ionization Detection in the SuperCDMS Experiment*, *Phys. Rev. Lett.* **112** (Jan., 2014) 041302, [[arXiv:1309.3259](#)].

- [7] E. Behnke, J. Behnke, S. J. Brice et al., *Improved Limits on Spin-Dependent WIMP-Proton Interactions from a Two Liter CF₃I Bubble Chamber*, *Phys. Rev. Lett.* **106** (Jan., 2011) 021303.
- [8] H. S. Lee, H. Bhang, S. Choi et al., *Search for low-mass dark matter with CsI(Tl) crystal detectors*, *Phys. Rev. D* **90** (Sept., 2014) 052006, [[arXiv:1404.3443](#)].
- [9] D. N. Spergel, *Motion of the Earth and the detection of weakly interacting massive particles*, *Phys. Rev. D* **37** (Mar., 1988) 1353–1355.
- [10] J. Billard, F. Mayet and D. Santos, *Assessing the discovery potential of directional detection of dark matter*, *Phys. Rev. D* **85** (Feb., 2012) 035006, [[arXiv:1110.6079](#)].
- [11] J. Billard, F. Mayet and D. Santos, *Markov chain Monte Carlo analysis to constrain dark matter properties with directional detection*, *Phys. Rev. D* **83** (Apr., 2011) 075002, [[arXiv:1012.3960](#)].
- [12] S. Ahlen, N. Afshordi, J. B. R. Battat et al., *The case for a directional dark matter detector and the status of current experimental efforts*, *Int. J. Mod. Phys. A* **25** (Jan., 2010) 1–51, [[arXiv:0911.0323](#)].
- [13] J. Billard, F. Mayet and D. Santos, *Low energy electron/recoil discrimination for directional Dark Matter detection*, *JCAP* **2012** (July, 2012) 020–020, [[arXiv:1205.0973](#)].
- [14] D. Santos, O. Guillaudin, T. Lamy, F. Mayet and E. Moulin, *MIMAC : A Micro-TPC Matrix of Chambers for direct detection of Wimps*, *J. Phys. Conf. Ser.* **65** (2007) 012012, [[astro-ph/0703310](#)].
- [15] F. J. Iguaz et al., *Micromegas detector developments for Dark Matter directional detection with MIMAC*, *JINST* **6** (2011) P07002, [[arXiv:1105.2056](#)].
- [16] I. Giomataris, R. De Oliveira, S. Andriamonje et al., *Micromegas in a bulk*, *NIMA* **560** (May, 2006) 405–408.
- [17] J. Richer, G. Bosson, O. Bourrion et al., *Development of a front end ASIC for Dark Matter directional detection with MIMAC*, *NIMA* **620** (Aug., 2010) 470–476, [[arXiv:0912.0186](#)].
- [18] O. Bourrion, G. Bosson, C. Grignon et al., *Data acquisition electronics and reconstruction software for directional detection of Dark Matter with MIMAC*, *Nucl. Instrum. Meth.* **A662** (2010) 207–214, [[arXiv:1006.1335](#)].
- [19] D. Schlegel, *TARGET Users Manual*. PTB report 6.42-05-2, 2005.
- [20] V. Gressier, G. Pelcot, J. Pochat and T. Bolognese-Milstajn, *New IRSN facilities for neutron production*, *NIMA* **505** (June, 2003) 370–373.
- [21] L. S. Waters, *MCNPX User’s manual version 2.3.0*. MCNPX, 2002.
- [22] R. L. Walker and B. D. Mcdaniel, *Gamma-ray spectrometer measurements of fluorine and lithium under proton bombardment*, *Phys. Rev.* **74** (Aug, 1948) 315–327.
- [23] O. Guillaudin, J. Billard, G. Bosson et al., *Quenching factor measurement in low pressure gas detector for directional dark matter search*, *EAS Publ. Ser.* **53** (Feb., 2012) 119–127, [[arXiv:1110.2042](#)].
- [24] J. Billard, F. Mayet and D. Santos, *Three-dimensional track reconstruction for directional Dark Matter detection*, *JCAP* **2012** (Apr., 2012) 006–006, [[arXiv:1202.3372](#)].
- [25] L. Breiman, J. H. Friedman, R. A. Olshen and C. J. Stone, *Classification and Regression Trees*. Taylor & Francis, 1984.

- [26] A. Hoecker, P. Speckmayer, J. Stelzer et al., *TMVA - Toolkit for Multivariate Data Analysis*, *PoS ACAT* **040** (Mar., 2007) 135, [[arXiv:0703039](#)].
- [27] S. Biagi, *Monte Carlo simulation of electron drift and diffusion in counting gases under the influence of electric and magnetic fields*, *NIMA* **421** (jan, 1999) 234–240.